Developing an Explainable Variational Autoencoder (VAE) Framework for Accurate Representation of Local Circulation in Taiwan

Min-Ken Hsieh[1] and Chien-Ming Wu[1]

[1] Department of Atmospheric Sciences, National Taiwan University, Taipei, Taiwan

Corresponding author: Chien-Ming Wu (mog@as.ntu.edu.tw)

Key Points:

- An Explainable artificial intelligence is constructed to capture Taiwan's local circulation using TaiwanVVM ensemble simulations.
- The representation of local circulation in the latent space of the VAE can be formulated as synoptic wind speed and direction.
- This framework can effectively generate accurate local circulation in Taiwan for fast climate response assessment.

Abstract

This study develops an explainable variational autoencoder (VAE) framework to efficiently generate high-fidelity local circulation patterns in Taiwan, ensuring an accurate representation of the physical relationship between generated local circulation and upstream synoptic flow regimes. Large ensemble semi-realistic simulations were conducted using a high-resolution (2 km) model, TaiwanVVM, where critical characteristics of various synoptic flow regimes were carefully selected to focus on the effects of local circulation variations. The VAE was constructed to capture essential representations of local circulation scenarios associated with the lee vortices by training on the ensemble dataset. The VAE's latent space effectively captures the synoptic flow regimes as controlling factors, aligning with the physical understanding of Taiwan's local circulation dynamics. The critical transition of flow regimes under the influence of southeasterly synoptic flow regimes is also well represented in the VAE's latent space.This indicates that the VAE can learn the nonlinear characteristics of the multiscale interactions involving the lee vortex. The latent space within VAE can serve as a reduced-order model for predicting local circulation using synoptic wind speed and direction. This explainable VAE ensures the accurate predictions of the nonlinear characteristics of multiscale interactions between synoptic flows and the local circulation induced by topography, thereby accelerating the assessments under various climate change scenarios.

Plain Language Summary

This research introduces an advanced neural network framework for generating high-fidelity local flow patterns in Taiwan. This framework, known as an explainable variational autoencoder, can accurately simulate how wind patterns of synoptic weather conditions interact in this region. We used detailed simulations to train the variational autoencoder, ensuring it captures the complex relationships between local flow and larger-scale weather patterns. By training on the detailed simulations, the variational autoencoder learned and represented these large-scale weather patterns in a way that helps maintain the physical relationship between local flow prediction and the large-scale weather patterns. One of the key outcomes of this study is the development of a reduced-order model. This simplified model takes advantage of what we have learned about complex weather interactions and can quickly predict local weather under different conditions. This approach ensures accurate predictions, even in complex situations involving changing climate conditions.

1 Introduction

The advances in data-driven Artificial intelligence (AI) /Deep Learning (DL) models for weather forecasting (e.g.Pangu-Weather (Bi et al., 2023), FourCastNet (Pathak et al., 2022) and GraphCast (Lam et al., 2022)) that significantly lower computational cost, offering a promising alternative to state-of-the-art numerical weather prediction (NWP) models. As the frequency and intensity of extreme weather events increase in the warming earth, deep generative models have garnered significant interest in meeting the demand for accurately assessing the intensity, timing, and spatial distribution of local extreme weather events, with a particular focus on generative adversarial networks (GANs) (Goodfellow et al., 2014). The applications of GANs are mostly gaining traction in the realm of extreme precipitation, such as estimating single-site precipitation patterns (Zadrozny et al., 2021), generating extreme precipitation (Bhatia et al., 2020),

reconstructing missing information in microwave precipitation data (Wang et al., 2021), and generating spatiotemporal weather patterns of extreme events (Klemmer et al., 2021). These research efforts exemplify the potential of deep generative models in addressing the challenges associated with extreme weather events and signify a promising direction for enhancing weather forecasting capabilities.

As an alternative, Variational Autoencoders (VAEs) (Kingma & Welling, 2014; 2019, hereafter KW2019) offer an encoder-decoder generative model that explicitly learns the distribution of the training set. By regularizing the latent space to a known distribution, VAEs enable stochastic synthesis that is primarily controlled by the latent space distribution. This allows researchers to identify where to sample from to achieve synthesis with specific desired characteristics. This property enhances the interpretability of VAE-based generative models. VAE applications have showcased their effectiveness in discussing weather fields in extreme scenarios, as demonstrated by Oliveira et al. (2021) and Behrens et al. (2022). Their results show that VAEs can skillfully reproduce subgrid cloud processes and reveal key cloud-type features. In addition, Shamekh et al. (2022) showed improved estimations of precipitation variability using VAE-learned low-dimensional variables for convection aggregation at the subgrid scale.

While deep generative models show progress in efficiently exploring the physics of geosciences, there remains a significant concern. Purely data-driven DL models might sometimes lack consistency in their predictions concerning established laws of physics (Daw et al., 2017). Additionally, the limited number of labeled instances available for training or cross-validation can often fail to accurately represent the underlying relationships in scientific problems (Karpatne et al., 2017). This concern becomes even more pronounced when applying DL models trained with current climate data to infer scenarios in a warming climate. The changing conditions and unique characteristics of a warming climate can lead to uncertainties and challenges in model generalization, raising questions about the reliability and robustness of data-driven approaches in such contexts.

The recent emergence of physics-informed neural networks (PINNs) has provided a promising approach to addressing the challenges of purely data-driven DL models. In a pioneering study, Beucler et al. (2021) introduced a climate-invariant machine learning approach that involves transforming the input/output features of the DL framework into a set of physical parameters with consistent distributions across different climates. Their findings demonstrated that incorporating physical considerations, even in the data preprocessing stage, can enhance the performance of DL models. This highlights the potential for bridging the gap between DL models and physics knowledge, thereby imposing physical constraints on model outputs and improving prediction skills for unseen scenarios.

In this study, we aim to utilize the neural network to address the evaluation of the local circulation induced by complex topography, which remains one of the most challenging aspects in global general circulation models (GCMs), even under sub-hundred-kilometer resolutions. Consequently, evaluating local responses to climate change often relies heavily on dynamical downscaling approaches. These approaches perform high-resolution numerical simulations to acquire detailed information on local phenomena under specific warming scenarios. However, the dynamical downscaling approach demands substantial computation resources and can introduce uncertainties, leading to the "cascade of uncertainty" in assessing the local responses to the various climate projections (Wilby and Dessai, 2010).

Taiwan provides a natural laboratory for studying AI downscaling where complex orography is generally underrepresented in current models even at kilometer scales. With nearly 200 summits surpassing 3000 m within its central mountain range, covering two-thirds of its total 36000 km^2 area, the island's complex topography interacts with large-scale synoptic conditions to induce a diverse array of local circulations. These local circulations control various weather phenomena, such as air pollution transport, which is well discussed in the literature (Lai and Lin, 2020; Hsieh et al., 2022, hereafter H2022; Hsu et al., 2023, hereafter H2023). These studies suggested that the local circulation can be dramatically different under the slight change of the synoptic flow regimes, and consequently impacts the air pollution scenarios in Taiwan. Figure 1 depicts the local pollution patterns as an indicator of the local circulation scenarios to demonstrate the impacts of the synoptic flow regime change on the local flow patterns. By carefully selecting local-circulation dominated days, which exclude the impact of long-range pollutant transport by cyclones, cold surges, and strong northeasterly winds in the highly-polluted cold season (Oct. to Apr.), the windrose in Fig. 1a reveals the variation of synoptic near-surface flow regimes near Taiwan (the average wind direction and speed below 925 hPa in the sounding data at Ishigaki island, Japan). We select the southeasterly flow regimes with a slight change in wind direction (wind direction veers from 120° to 150°) to display the $PM_{2.5}$ pollution scenarios bifurcation as shown in Fig. 1b and Fig. 1c, named as WD120 and WD150 flow regimes respectively. For each distinct flow regime, we chose cases where the synoptic wind directions fell within a 30-degree range and the wind speeds were limited to a 2 m s^{-1} range (as shown in the titles of Fig. 1b and 1c). The dots over Taiwan in Fig. 1b and 1c are color-coded based on the enhancement index, which considers the historical frequency of observed aerosol concentration exceeding the 12-year average that can exclude the effects of uneven local emissions as suggested by H2023. Figure 1b (1c) shows that the $PM_{2.5}$ pollution deteriorates over the south (north) Taiwan around Kaohsiung (Taipei) while the pollution on the north (south) corner near Taipei (Kaohsiung) is alleviated. The contrast between Fig. 1b and Fig. 1c demonstrates that the local pollution scenarios can be significantly changed by only a 30° shifting of the synoptic prevailing wind direction. Despite the aforementioned studies confirming that local circulation plays a crucial role in linking large-scale flow regimes to local pollution patterns, obtaining detailed information about local circulation requires computationally intensive physical numerical models, as shown in a case study by Lin et al. (2022).

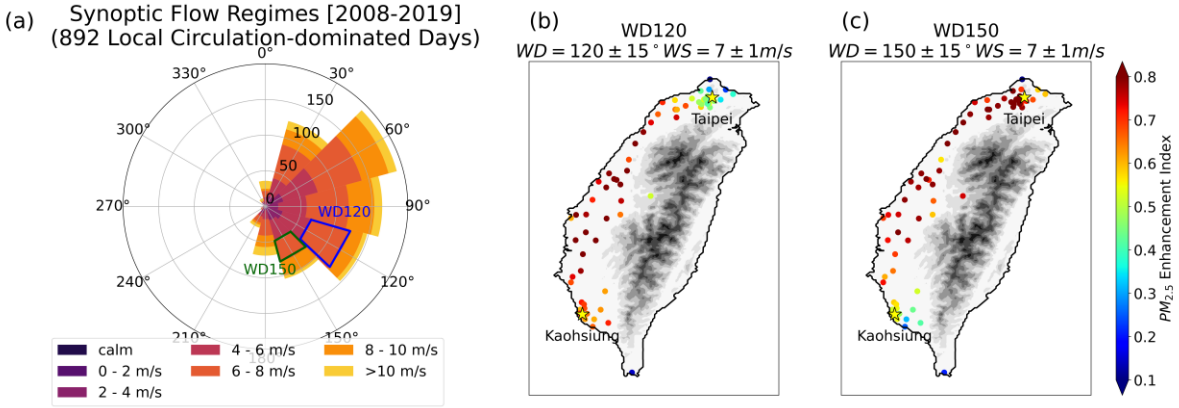

Fig 1. The local pollution scenarios controlled by the synoptic flow regimes. (a) The frequency distribution of synoptic flow regimes in the local circulation-dominated days in the cold season (Oct. to Apr.) from 2008 to 2019. (b) The $PM_{2.5}$ pollution enhancement index under WD120 synoptic flow regimes indicated by the blue bracket in subfigure (a).

(c) The $PM_{2.5}$ pollution enhancement index under WD150 synoptic flow regimes indicated by the green bracket in subfigure (a). The yellow asterisks in (b) and (c) indicate Taipei and Kaohsiung city, Taiwan's major cities.

In this study, we propose the generation of local circulation using an explainable VAE framework trained by the large ensemble dataset from the numerical simulation focusing on the specific pollution weather regime as mentioned above. The physically constrained training dataset allows the VAE to learn the nonlinear physical relationship between the local circulation and the upstream synoptic flow regimes. To capture the multiscale interaction between synoptic conditions and local circulations over complex terrain, we employ the high-resolution physics model, TaiwanVVM (Wu et al. 2019, hereafter W2019), to generate a physically constrained dataset. Leveraging the semi-realistic TaiwanVVM simulation framework, we conduct an ensemble of simulations to generate detailed local circulation scenarios under various synoptic forcing regimes in observations. The ensemble of high-dimensional simulations serves as an analogy of the large-eddy-simulation library driven by large-scale forcing that expands the dataset in various synoptic regimes available for DL approaches learning from (Shen et al., 2022).

By employing this dataset, a VAE model is trained ensuring that the model learns physically consistent solutions. We show that the 2-dimensional latent space of the VAE well captures the variability of the local circulations associated with the lee vortices in the training data, and the trained VAE can generate realistic local circulations. The manifold provided by VAE is further interpreted as the physical parameters of upstream flow regimes that drive the variability of the local flows in the training data, which is aligned with understanding of the leeside local circulation formation mechanism. Consequently, in conjunction with the decoder, the physically-interpreted manifold can function as a reduced-order model that can generate the high-fidelity local circulation induced by the topography of Taiwan with high efficiency.

Our approach emphasizes that VAE can learn fluid dynamics through training on a large ensemble of LES that captures the large-scale variability of the controlling factors on a specific fluid phenomenon, such as the leeside flow structure in this study. Given the large-scale conditions, the reduced-order model derived from the VAE can predict high-resolution local circulation under various climate change scenarios. To demonstrate the capability of this framework, we apply the reduced order model to downscale the crucial synoptic flow pattern change at the end of the century in the climate projection from a member of Coupled Model Intercomparison Project Phase 6 (CMIP6, Eyring et al., 2017), namely Taiwan Earth System Model Version 1(TaiESM1, Lee et al., 2020). The generated local circulations provide a physical fundamental to predict the potential pollution deterioration in the major cities of Taiwan. The manuscript is organized as follows. The TaiwanVVM semi-realistic ensemble dataset and the construction of the explainable VAE framework are described in section 2. The results and their physical interpretation are depicted in section 3, followed by the application of the reduced-order model and discussion in section 4.

2 Data and Methods

2.1 Semi-Realistic TaiwanVVM Simulation Dataset

To incorporate physical consistent data as the training dataset of the VAE framework, we employ a physical model known as TaiwanVVM (W2019) to generate physics-constrained training data. TaiwanVVM is a simulation framework based on the Vector Vorticity equation cloud-resolving Model (VVM, Jung and Arakawa, 2008), featuring a realistic representation of Taiwan's topography using the immersed boundary method (Wu and Arakawa, 2011; Chien and Wu, 2016). This model has been extensively utilized in studies concerning local precipitation hotspots (Kuo and Wu, 2019; Chang et al., 2021, hereafter C2021). A series of studies focused on the local pollution distribution scenarios also suggested that the TaiwanVVM model can evaluate the variability of the lee vortices flow patterns under various synoptic prevailing wind conditions (H2022; H2023). These studies have demonstrated the model's capability to capture comprehensive information about the local circulation and highlighted its reliability and suitability for generating physics-constrained training data for the VAE framework. The TaiwanVVM framework details are presented in Table 1. The simulation starts at 6:00 local time with a 24-hour duration so that the diurnal local flows induced by the heating difference over the complex topography can develop and further interact with the large-scale prevailing winds. The overall simulation setup follows H2022 while relaxing the horizontal and vertical resolution to enlarge the simulation domain that better covers the entire lee side local circulations while remaining to resolve the crucial flow structures we focus on.

Table 1. TaiwanVVM simulation framework

Horizontal Resolution	2 km
Vertical Resolution	46 m near surface and stretch up to 969 m at model top
Land Surface Model	Noah Land Surface Model version 3.4.1 coupled with land type and topography of Taiwan (Wu et al., 2019)
Representation of topography	Immersed boundary method with block mountain in height coordinate (Wu and Arakawa 2011; Chien and Wu 2016)
Lateral Boundary Condition	Double periodic

To generate realistic local circulations under various synoptic conditions using VAE, it is essential to introduce the variability of synoptic conditions into the simulation of the physics model. To address this, we adopt a semi-realistic simulation framework proposed in C2021, employing sounding observations as uniform initial conditions across the entire domain. This approach emphasizes the influence of controlling environmental factors that govern the development of local circulations. We utilize sounding observations from Ishigaki Island, Japan, to represent the synoptic conditions in the semi-

realistic simulations. Figure 1a illustrates the variability of synoptic flow regimes on days dominated by local circulation, showing that prevailing winds are primarily confined to northeasterly and southeasterly directions. This observation aligns with the assumption that Ishigaki Island is located upstream of Taiwan. Subsequently, we extend the selection of local circulation-dominated days from 1980 to 2020, subjectively choosing 197 out of a total of 2893 days to conduct the large ensemble TaiwanVVM simulations. By incorporating the variability of the synoptic environment, our semi-realistic simulation framework accounts for the diverse local circulations resulting from the interaction between synoptic forcing and the physical effects of topography, including diurnal heating differences and the blocking of prevailing flow. This physics-constrained ensemble dataset is then prepared for representation learning using the VAE.

2.2 Variational Autoencoder

Autoencoder (AE) is a specific neural network architecture distinguished by its unique bottleneck structure. This feature endows AEs with the capability of performing effective nonlinear dimension reduction, making it a valuable tool in geoscience applications that often seek the crucial features or coherent structures within patterns in considerable volumes of data. Operating as an unsupervised representation learning framework, AEs excel at extracting the essential hidden manifold that optimally captures the variability present in the input data. However, the pitfall of AEs is that the latent space is constrained solely by the reconstruction loss. Minimizing reconstruction error tends to obtain an overfitting AE, in which fair reconstruction results are accompanied by the latent space that is only partially defined and incomplete. The gaps between the points representing the training data in the latent space are undefined, which means that the manifold is not continuous and does not allow interpolation, leading to the incapability of physical interpretation. The VAE proposed by KW2019 offers a solution to the challenge of unregulated latent spaces within AEs while also introducing generative capabilities across the entire space. The VAE's encoder generates parameters for a predefined distribution within the latent space. Subsequently, the VAE enforces a constraint on this latent distribution to adhere to a normal distribution. A brief description of VAE following KW2019 is provided below.

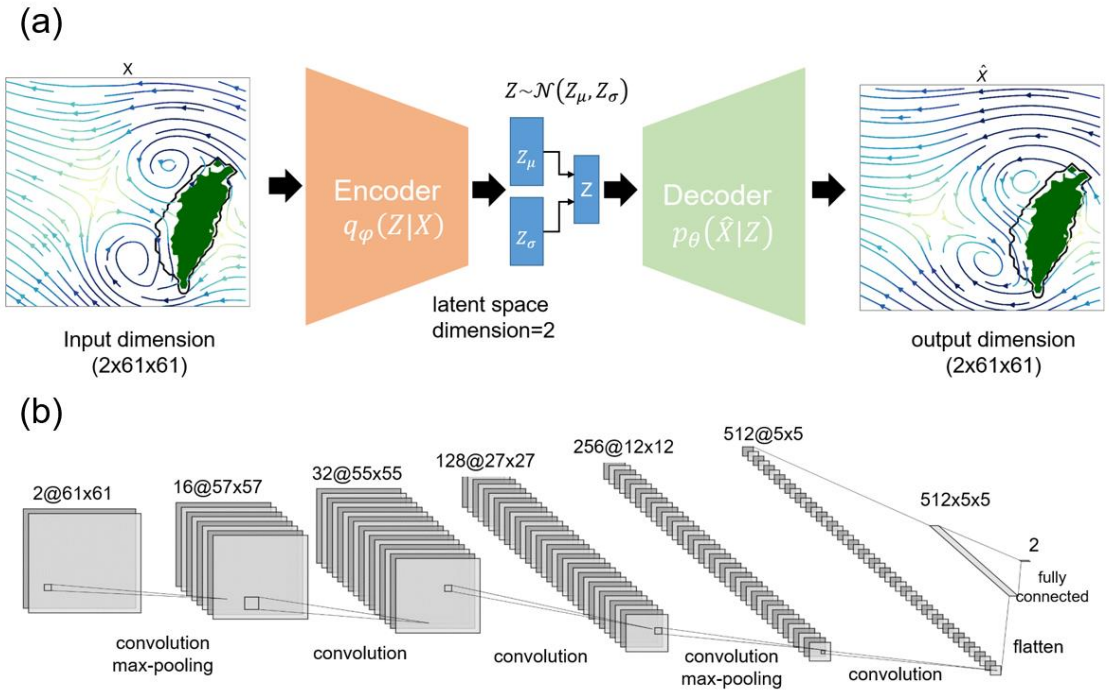

Fig. 2 The convolutional variational autoencoder framework. (a) The schematics of variational autoencoder framework. (b) The design of the convolutional encoder.

To replace the deterministic latent variables employed in AEs with latent distributions, as illustrated in Fig. 2a, the encoder within the VAE is conceptualized as a probabilistic encoder. Its primary function involves estimating the posterior probability of latent vectors Z given observed input X and parameterized by θ, denoted as $p_\theta(Z|X)$. However, as pointed out by KW2019, $p_\theta(Z|X)$ is usually intractable or excessively intricate. Consequently, the encoder functions as an inference model, aiming to identify a surrogate distribution, $q_\varphi(Z|X)$, that effectively approximates the posterior of these intricate latent distributions parameterized by φ. Thus, to achieve this approximation, the Gaussian distribution is commonly chosen as the form for the approximate posterior distribution. By leveraging encoder-derived parameters for mean Z_μ and variance Z_σ the approximate posterior distribution $\mathcal{N}(Z_\mu, Z_\sigma)$ is formulated. By introducing the Kullback-Leibler (KL) divergence, a quantification of the closeness between two distributions, we can gauge the dissimilarity between our normal distribution characterized by parameters Z_μ and Z_σ, and the prior distribution. Notably, as discussed by KW2019, the calculation of the KL divergence possesses a closed-form expression when assuming the standard Gaussian distribution $\mathcal{N}(0,1)$ as the prior distribution:

$$D_{KL}[\mathcal{N}(Z_\mu, Z_\sigma)||\mathcal{N}(0,\mathrm{I})] = -0.5\sum_{i=1}^{N} 1 + \log\left({Z_{\sigma_i}}^2\right) - {Z_{\mu_i}}^2 - {Z_{\sigma_i}}^2 \quad (1)$$

In Equation (1), the summation encompasses all N dimensions within the latent space. Utilizing the logarithm of variance in computing the KL divergence is preferred to facilitate an output range comprising natural numbers rather than solely positive values. This choice promotes smoother representations of the latent space. Including the KL

divergence within the VAE's loss function bestows it with a regularization role, ensuring alignment of the latent distribution with a normal distribution. Consequently, this enforces a more structured and well-controlled depiction of the latent space.

Within the VAE framework, as visually depicted in Fig. 2a, the latent variable vector Z is sampled from the latent distribution. This distribution is parameterized by the mean and standard deviation outputted from the encoder. Subsequently, the latent variable vector Z is input into the decoder to generate the desired output. This stochastic sampling procedure can be described as follows:

$$\mathrm{Z} \sim \mathcal{N}(Z_\mu, Z_\sigma) \quad (2)$$

In the gradient-based training procedure of VAE, the loss derived from the outputs necessitates backward propagation across the entire network for parameter refinement. However, this random sampling process creates a bottleneck as gradients cannot effectively propagate through the sampling layer. Consequently, this limitation impedes the learning of parameters Z_μ and Z_σ. To address this challenge, KW2019 devised a reparameterization trick, which reformulates Equation (2) as follows:

$$\mathrm{Z} = \mu + \sigma \odot \epsilon$$
$$\epsilon \sim \mathcal{N}(0,1) \quad (3)$$

In Equation (3) the $\odot$ donates elementwise multiplication and the latent variable vector Z is calculated by a fixed mean Z_μ plus the fixed standard deviation Z_σ scaled by a random sampled ϵ from unit Gaussian distribution. This rearrangement achieves the same outcome as the random sampling process described in Equation (2). Importantly, this reparameterization converts the calculating of Z, involving Z_μ and Z_σ, into deterministic nodes. Consequently, this adjustment enables the seamless passage of gradients, ensuring effective gradient backpropagation throughout the network.

As the reparameterization trick adopted to preserve the stochasticity in the decoder and the KL divergence in Equation (1) introduced as a regularization loss, KW2019 successfully showcased the feasibility of constructing a VAE framework. This framework enables the establishment of a continuous end-to-end training process aimed at extracting the latent distribution from the given data. Within the context of this study, the loss function for the VAE is formulated as follows:

$$loss_{VAE} = loss_{reconstruction} + \beta loss_{regularization}$$

$$= \sum_{x \in \mathrm{X}} \|x - \hat{x}\| + \beta D_{KL}[\mathcal{N}(Z_\mu, Z_\sigma) || \mathcal{N}(0, \mathrm{I})] \quad (4)$$

The first term in Equation (4) is reconstruction loss, aiming to attain high-quality reconstruction akin to the loss definition in the conventional AE. The reconstruction loss assesses the fidelity of the reconstructed data, where x represents a sample, and $\hat{x}$ represents its corresponding reconstruction. The second term corresponds to the KL divergence penalty, serving to regularize the latent space, as elaborated earlier. In order to achieve an optimal equilibrium between the precise reconstruction of the input data and the acquisition of meaningful representations within the latent space, we introduced a parameter β governing the weighting applied to the regularization loss. By incorporating Equation (1) and opting for the mean square difference as the reconstruction loss metric, we can formulate Equation (4) as follows:

$$loss_{VAE} = \frac{1}{M}\sum_{k=1}^{M}(x_k - \hat{x}_k)^2 + \beta(-0.5\sum_{i=1}^{N} 1 + \log\left({Z_{\sigma_i}}^2\right) - {Z_{\mu_i}}^2 - {Z_{\sigma_i}}^2) \quad (5)$$

In Equation (5), M refers to the amount of the training samples and N represents the latent dimensions. By minimizing this loss metric during the training process, the regularized latent distribution can be taken as a complete and continuous representation of the variability in the training dataset with only N dimensions. It is always desired to gain a representation of the variability in atmospheric data with only a few dimensions since the spatial-temporal variations of atmospheric phenomena are usually displayed by data with hundreds or thousands of dimensions. The complete and continuous representation can also be elaborated in a more physical sense. Moreover, the VAE as a generative model can generate new high-dimensional data by sampling the learned latent distribution. This functionality creates an opportunity for constructing a reduced-order model for predicting local circulation with high efficiency. In the next subsection, we elaborate on the construction of the explainable VAE framework that binds the semi-realistic ensemble simulations to the VAE.

2.3 Explainable VAE Framework

In this study, we aim to construct a DL generative model that can physically evaluate the local circulation of Taiwan. While the idealized tracer transport simulation study confirmed that the synoptic prevailing flow regime is crucial in controlling the local circulation patterns of Taiwan (H2022), the nonlinear critical transition of the local circulation scenarios under the synoptic conditions in the real world, as depicted in Fig. 1, still needs further evaluation. We conducted the semi-realistic TaiwanVVM ensemble simulations as depicted in 2.1 to encompass the variability of the local circulation scenarios under various synoptic conditions. By taking the ensemble dataset as the training data, we incorporate the underlying physics from the TaiwanVVM model into the representation learning process of the VAE.

From a total of 197 simulations, we collected output wind field snapshots within an 18-hour span starting from 8:00 local time with a 20-minute frequency as the VAE training data. This selection enables the inclusion of the local circulation's diurnal evolution while excluding the first two hours for model spinning-up. The snapshot of simulated 3-dimensional wind fields is a massive volume, making it a challenge as a single training example. To address this issue, we strategically focused on the near-surface horizontal winds at the lowest level over the west plain of Taiwan in the simulation (160 m above sea level) as a surrogate of the local circulations. These horizontal wind fields exhibit distinct scenarios under various synoptic flow regimes. To further manage the data size, we trimmed the horizontal spans of the 2-dimensional wind fields to a subspace of the entire domain and downsampled them to a 10-km resolution where the wake of the prevailing synoptic flow is present. The 10-km resolution horizontal wind field from the ensemble simulation results serves as the training data for the VAE. This dataset comprises u-wind and v-wind components in a 61×61 horizontal grid with a total of 9456 samples for the representation learning in VAE as displayed in Fig. 2.

Utilizing a dataset comprising 9456 physically constrained samples, we construct the encoder and decoder of the VAE employing five convolutional layers. The convolutional architecture of the encoder is displayed in Fig. 2b, while the decoder is the reverse setup with deconvolution layers. The convolutional layers are designed to effectively capture spatial features inherent in the local circulation patterns present within

the training data. The hyperbolic tangent function was employed as the activation function across all layers, ensuring the output of each layer is confined within -1 to 1. By testing the effects of the scaling parameter of the regularization KL divergence β in Equation (5), we found that the VAE cannot reconstruct the various input local circulations when β exceeds 0.2. We select the β as 0.1 to gain the fair reconstruction under a mild regularization. For the choice of latent dimension N, a 3-dimensional latent space of AE shows that most of the projected points of the training data are gathered on a plane, indicating that a 2-dimensional latent space is sufficient to capture the variability of the training samples. As a result, we set the latent dimensions N as 2 to conduct the training procedure. We used the Adam optimizer with a learning rate of 0.001, We trained the models for 1000 epochs. All experiments were carried out using Nvidia GP100 GPUs.

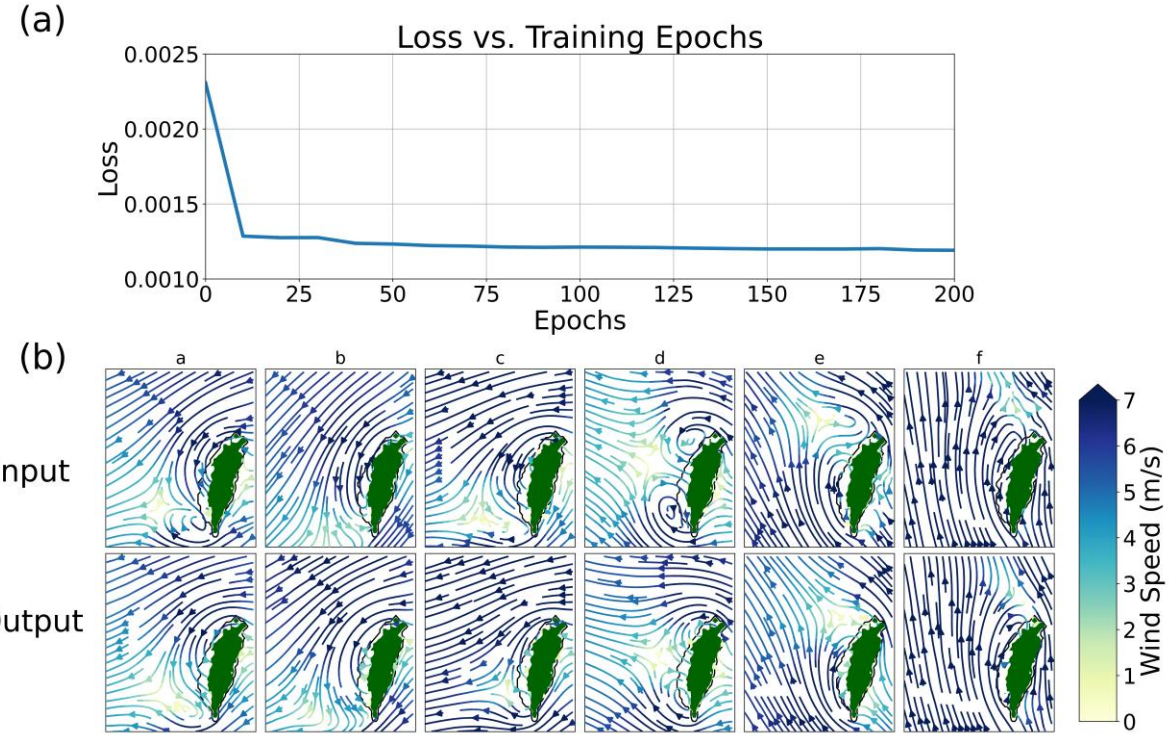

Fig. 3 The training results of the VAE. (a) The decrease of loss in the training process in the first 200 epochs. (b) The comparison of local circulations reconstructed by VAE and the original input data in 6 samples. The local circulations are displayed as the streamlines, and the color represents the wind speed (m/s). The green shedding area indicates the mountain areas of Taiwan where the ground level is above 200 m. The upper row displays the input training data in these 6 samples, the corresponding reconstruction outputs are shown in the same column of the lower row.

The training results are summarized in Fig. 3. Figure 3a illustrates the progressive decrease of the total loss in the first 200 epochs of the training procedure. These training iterations exhibit an initial rapid reduction of the loss within the first 100 epochs, followed by a slight decline to levels below 0.0012 with fluctuations to the end of training. By meticulously minimizing the loss, the VAE undergoes training to accurately reconstruct diverse local circulation training samples, as shown in Fig. 3b. The subfigure

columns, ranging from "a" to "f" in Fig. 3b, showcase distinct local flow patterns corresponding to the shifting synoptic flow regimes. As the prevailing wind direction changes from northeasterly to southeasterly, the local flow structure over Taiwan's western region undergoes a transition from a pronounced northerly pattern with a reverse flow located at the southwest of Taiwan (column "a" in Fig. 3b) to a dipole configuration of lee vortices (column "d" in Fig. 3b), and ultimately to a more prominent southerly accompanied with the reverse flow near northern Taiwan scenario (column "f" in Fig. 3b). This sequence of evolving scenarios highlights the dynamic multiscale interaction between synoptic conditions and local flow patterns. Importantly, the training samples (the upper row of Fig. 3b) distinctly display the flow structure of lee vortices with these varying scenarios, affirming the effectiveness of our training data extraction methodology in addressing the challenge of high-dimensional data, while successfully preserving the fundamental attributes of the local circulation patterns as derived from the physical model.

In addition, the comparison between input samples (the upper row of Fig. 3b) and their corresponding reconstructed local circulations (the lower row of Fig. 3b) indicates that the VAE adeptly encompasses the coherent structures of the local circulations which are presented within the input data. Given that the core attributes of the local circulation remain intact in the reconstruction outputs, it can be inferred that the latent space derived from the VAE captures the essential representation of the local circulation. Notably, the assessment of the reconstruction also underscores the distinctive aspect of the VAE as a deep generative model. While other deep generative models such as GAN can produce a synthetic output through the random sampling process, their sampling distribution often comprises pre-defined Gaussian noise that is irrelevant to the generating performance. For example, the training process of GAN is reinforced through the competition between the discriminator and generator, yielding improved results while incapable of exploring the hidden structures of the training data. In contrast, VAEs are explicitly designed to uncover hidden manifolds through the training data. The success of reconstruction can be attributed to the VAE's ability to capture the training samples via latent distributions. To explore the capability of VAE to infer the physical meaning of the training data, we inspect the latent space of the trained VAE in the next section.

3 Results

As the VAE is capable of reconstructing realistic local circulations akin to the input data, we further examine the robustness of the VAE by inspecting the various local circulations generated from the latent space. As 88.5% of the latent vectors of the training data are gathered within the $x \in [-2,2], y \in [-2,2]$ subspace in the latent space, we focus on this area of latent space for further examination. By evenly sampling this subspace, we generate a matrix of the local circulation as displayed in Fig. 4. The sampling locations in the latent space are indicated in the titles of subfigures in Fig. 4. The entire local circulation matrix shows the continuous variations of the various local circulations, which is attributed to the normal distribution of the latent vectors regularized in VAE. As the latent vectors sampling locations near the left edge of the $x \in [-2,2], y \in [-2,2]$ subspace (Figs. 4a, e, i, m), the decoder can generate distinct local circulation associated with the lee vortices accompanied by different prevailing flows from southeasterly to northeasterly. For example, the generative local flow from point (x=-1.5, y=1.5) of the latent space shows that the signature of the local flow under the prevailing southeasterly is the presence of circular flow patterns associated with lee vortices in the wake of mountains and the

acceleration zones on the rear of the north and south capes of the topography (Fig. 4a). As the sampling point moves toward the lower left corner (x=-1.5, y=-1.5) of the latent space, the generating local flows turn into a profound northeasterly with lee vortex circulation located on the southwest of Taiwan (Fig. 4m). Furthermore, upon comparing the upper row (Figs. 4a to 4d) with the lower row (Figs. 4m to 4p) of the local circulation array, it becomes evident that the local circulations in the lower row exhibit a notably consistent pattern, while the upper row displays a distinct transition. This transition manifests as a shift from a dipole pattern of lee vortices under prevailing southeasterly conditions (Fig. 4a) to a milder anti-cyclonic curved flow pattern in a southerly environment (Fig. 4d). These findings illustrate that the generation process, using evenly sampled locations in the latent space, can effectively reproduce the nonlinear transitions observed in local circulations.

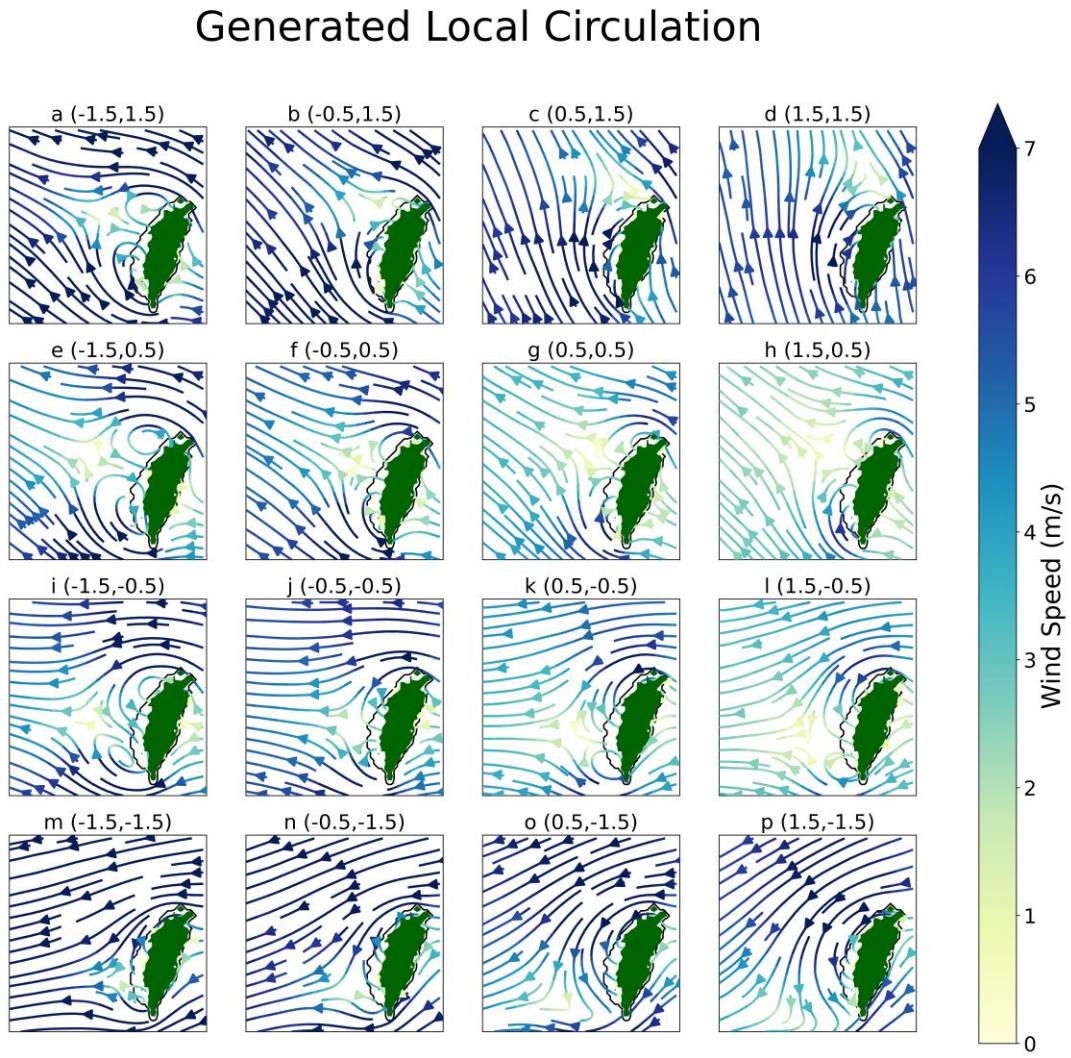

Fig. 4 The local circulations generated by evenly sampling the latent space. The sampling points of the latent space are titled in the subfigures.

Examining the variability in the generated local flows suggests that the VAE can produce reasonable local circulations under various specific prevailing winds. The essential low-dimensional latent distributions well capture the change in the prevailing flow regimes and the subsequent local circulations. It implies that the variability in local flows corresponding to different flow regimes embedded in the training data has been learned by the VAE through the training process. As we constrain the training data as the semi-realistic ensemble simulation results, the ensemble spread could be crucial clues for interpreting the latent space. In the TaiwanVVM simulation procedures, we prescribed the sounding observations as the initial conditions in the selected 197 local circulation-dominated cases to conduct the semi-realistic ensemble simulations. We take the near-surface (below 925 hPa) prevailing mean wind speeds and directions as the physical parameters of these simulations to discuss the physical implication of the latent space since the variability of the local circulations is controlled by the synoptic low-level flow regimes, as evidenced by the idealized simulations in H2022. The latent vectors of the training samples color-coded by the physical flow regimes are displayed in Fig. 5. The latent vectors spanned in the two-dimensional latent space, after being colored by corresponding initial synoptic wind speeds and directions of individual semi-realistic simulations, demonstrate that the lower-dimensional representations of the various local circulations are generally associated to their synoptic flow regimes. The latent vectors of the training samples induced by the synoptic southerly (darker colors in Fig. 5a) are projected in the upper right corner of the latent space, as shown in Fig. 5a. The lower half of the latent space is clustered of the latent vectors that represent the local circulations under the prevailing synoptic northerly to northeasterly (from 20° to 80° roughly) in the TaiwanVVM simulations. The training samples of the local circulations associated with the easterly synoptic winds occupy the middle and left parts of the latent space. As the various synoptic wind directions can be identified in the latent space, Fig. 5b also displays that the latent vectors resulting from different synoptic wind speeds are clearly separated., The latent vectors in the area of $x \in [1,2]$, $y \in [-0.5,0.5]$ are compressed from the local circulations induced by weak wind conditions (synoptic wind speed is less than 4 m s^{-1}), whereas the latent vectors projected to the upper-right or lower-right corner represent the local circulations in the simulations of stronger synoptic wind conditions.

The results show that different characteristics of the prescribed synoptic winds of the simulations are separated in the latent space of VAE, highlighting the role of synoptic variability on the local circulations. The shift in the latent space could be depicted as the gradual changes in synoptic flow regimes. We take advantage of the VAE that constrains the latent space as a continuous space to depict the variability of the local circulation in the semi-realistic ensemble dataset. As the various responses of the local circulation scenarios controlled by the different synoptic controlling factors are captured in the semi-realistic ensemble simulations, the VAE successfully learned this physical representation of the variability of local circulations in Taiwan and consequently secures the transparency of this framework through the interpretable latent space.

Within the physically-interpreted latent space, it is worth noting that the sharp transition of the generated local circulations, as shown in the top row of Fig. 4, can be attributed to the synoptic southeasterly flow regime, which is displayed as the dots near the top boundary with darker colors in Fig. 5. The sharp transition of the generated local circulations (Figs. 4a to 4d) by moving the sampling point from point (x=-1.5, y=1.5) to point (x=1.5, y=1.5) in the latent space can be elaborated as the shifting of the synoptic prevailing wind direction from about 120° to 160°. It shows that the VAE learned from the semi-realistic ensemble simulation dataset is

capable of generating a critical transition of local circulations under the gradual varying of the synoptic flow regimes.

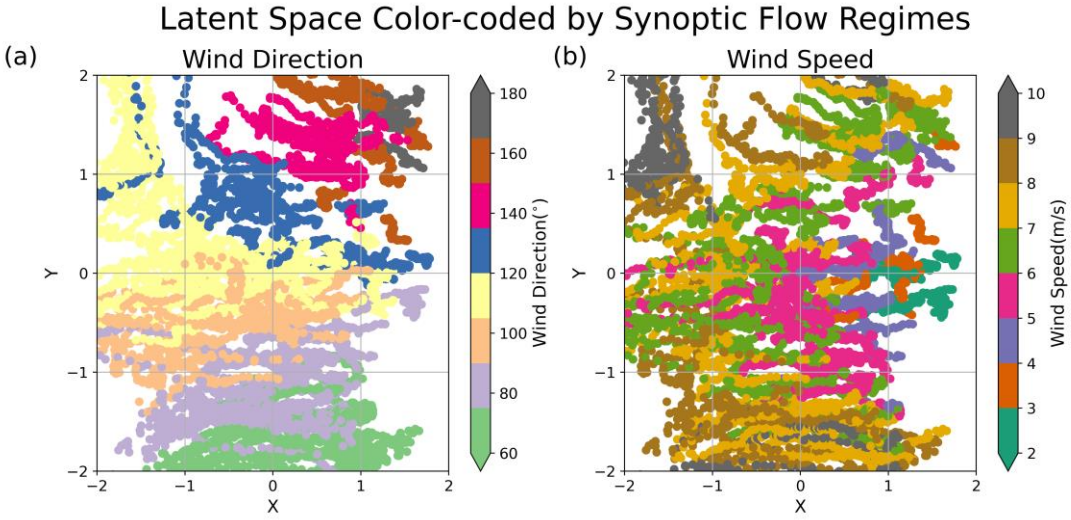

Fig. 5 The latent vectors of the training samples color-coded by (a) the synoptic wind directions and (b) the synoptic wind speeds.

As we constrain the training dataset of VAE through the physical simulations with the semi-realistic experiment design focusing on the topographically induced local circulation of Taiwan, the nonlinear compression functionality of the VAE can greatly reduce the complexity of multiscale interaction phenomena in atmospheric fluid dynamics. The resulting latent space with physical meaning, along with the decoder as a generative model, can serve as a reduced-order model that elaborates the pattern of the local circulation under a specific synoptic flow regime. To achieve this goal, we quantify the distribution of the representative synoptic flow regimes in the latent space using linear interpolation and simple least square curve fitting. The selection of fitting function forms is inspired by the visualization of the interpolated parameters in the latent space, as shown in Fig. 5. As the wind speeds of the latent vectors are distributed radially, and the wind directions vary along the y-axis, we select the elliptical and linear function forms to transform the orthogonal coordinates of latent space to the synoptic wind speed and direction, as follows:

$$WD = a + b\tan^{-1}\left(\frac{cy}{x-d}\right) \quad (6)$$

$$WS = a(x-\alpha)^2 + b(y-\beta)^2 \quad (7)$$

where *x* and *y* denote the cartesian coordinates of the 2-dimensional latent space, and a, b, c, d in Equation (6), and a, b, α, β in Equation (7) are the fitting parameters.

Figure 6a illustrates the contours of the fitting functions of synoptic wind directions and speeds within x∈[-2,4],y∈[-3,3] subspace in the latent space (details of the fitting parameters are depicted in the figure captions of Fig. 6a). With the mean absolute errors of the transformation confined to 0.71 m s^{-1} in wind speed and 5.76° in wind direction, the 2-dimensional latent space is spanned by synoptic flow regimes. The weak wind regime is located near the center of the right boundary, while the strong wind flow regimes are distributed toward the other boundaries. The synoptic northerly/northeasterly regimes occupy the lower half of the latent space, and the southeasterly/southerly synoptic flows can be identified on the upper half of the plane. While higher-order fitting functions can minimize fitting errors, we aim to demonstrate the capability of

the VAE to transform the latent space into physical parameters-based coordinates while maintaining the simplicity of the entire framework. Through this transformation, the new coordinates of the latent space can fulfill the alignment with the variability in the training samples represented by the latent vectors and offer a physical explanation of the latent distributions that can generate the high-fidelity local circulations.

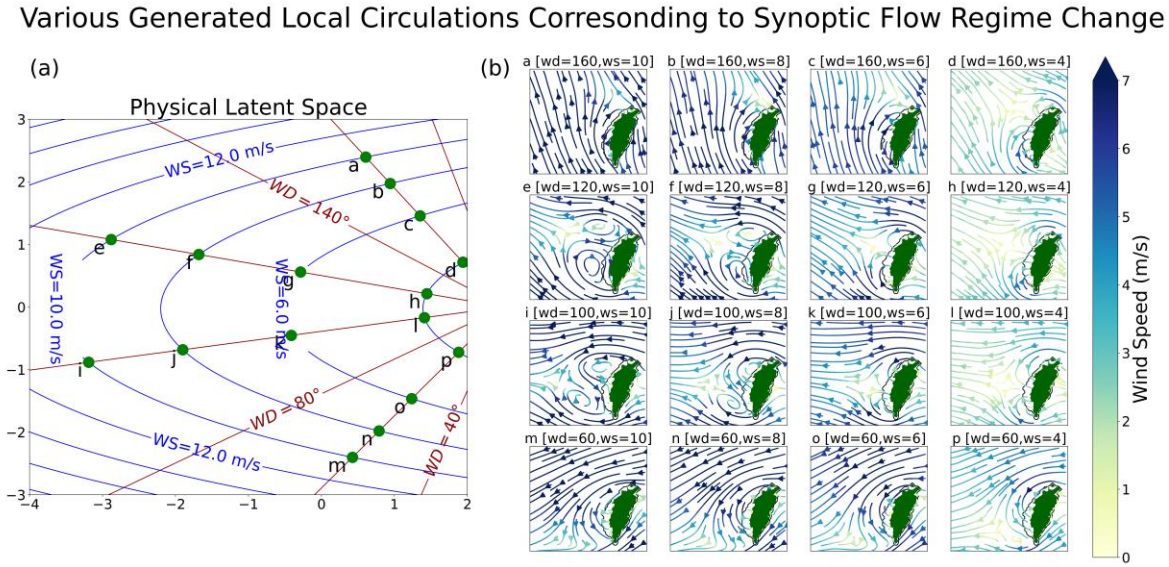

Fig. 6 (a) The contours of the synoptic wind direction (red lines) and wind speed (blue lines) derived by the fitting functions. The fitting function forms are selected as Equation (6) and Equation (7), where the fitting parameters for the wind direction fitting function are a=118.7, b=0.99, c=1, d=2.5, and the parameters are a=0.05, b=0.89, α=10.06, β=0.02 for the wind speed. (b) the generated high-fidelity local circulations. The local circulations correspond to the sampling points (green dots in subfigure (a)) in the latent space are shown in the titles of subfigures in (b) along with the synoptic wind directions and speeds.

By taking the latent space as a synoptic flow regime phase diagram, we construct the matrix of generated local circulations corresponding to the gradual changes in the synoptic flow regimes, as shown in Fig. 6b. The sampled locations in the latent space are selected as specific synoptic flow regimes that veer from southeasterly (on the upper half of the latent space) to northeasterly (on the lower half of the latent space), as well as the intensification of the prevailing wind speed (moves along the red lines in Fig. 6a from the central area near the right boundary to other boundaries radially). The corresponding variability of local circulations in the matrix (Fig. 6b) displays the reasonable scenarios in lee vortex flow structures. Upon examining the variation among the rows of the local circulation matrix, we can identify the impact of changes in wind direction. Notably, prevailing easterly winds tend to result in a dipole structure of the lee vortices on the west plain of Taiwan (Fig 6b-h and 6b-l). Moreover, when the prevailing wind direction shifts to southerly (northerly), it promotes the formation of cyclonic (anti-cyclonic) lee vortices, as evident in Fig. 6b-d (Fig. 6b-p). In addition, the effects of changes in synoptic wind speed are demonstrated through the local circulations across different columns of the matrix. Instances of the lee vortices stalling near the topography can be observed in Fig.

6b-h and 6b-g; the lee vortices tend to be shedding away from the topography as the prevailing winds intensified, as shown in Fig. 6b-f and 6b-e.

The compelling outcomes of the VAE serve as a valuable reduced-order model capable of generating local circulation from specific synoptic flow regimes, thereby conserving computational resources compared to the integration of traditional physics models. This approach showcases the potential of VAE as an effective AI downscaling tool for advancing our evaluation of complex local circulation under various climate change scenarios in the warming climate, in which the physics fundamental and the explainaibility are upmost essential demands.

4 Applicaiton and Discussion

In this study, we employed the VAE to learn the physical mechanism of the vortex formation of Taiwan in the semi-realistic TaiwanVVM simulations. The selection of suitable synoptic environments and the subsequent physics model simulation procedures served as essential physical preprocessing steps for the machine learning framework. The VAE excels in nonlinear dimension reduction of high-dimensional dynamic fields in the atmospheric domain, allowing us to extract essential features from the complex atmospheric data. Meanwhile, the TaiwanVVM simulation results adhere rigorously to physical laws and provide a robust foundation for the VAE to learn the physical representations of the variability in the local circulations in Taiwan. Through this integration of machine learning and physics-based simulations, we gained valuable high-fidelity local circulation through the VAE that can be explained physically.

As the VAE takes these physically constrained training data to learn from and further create a continuous phase diagram that can elaborate the variability in the training samples in terms of the synoptic conditions of the ensemble simulations, the VAE has yielded a reduced-order model capable of producing realistic and high-fidelity local circulation patterns in response to specific synoptic flow regimes. To demonstrate the application of the reduced-order model in examining the local weather, we revisit the $PM_{2.5}$ deterioration scenarios shown in Fig.1.

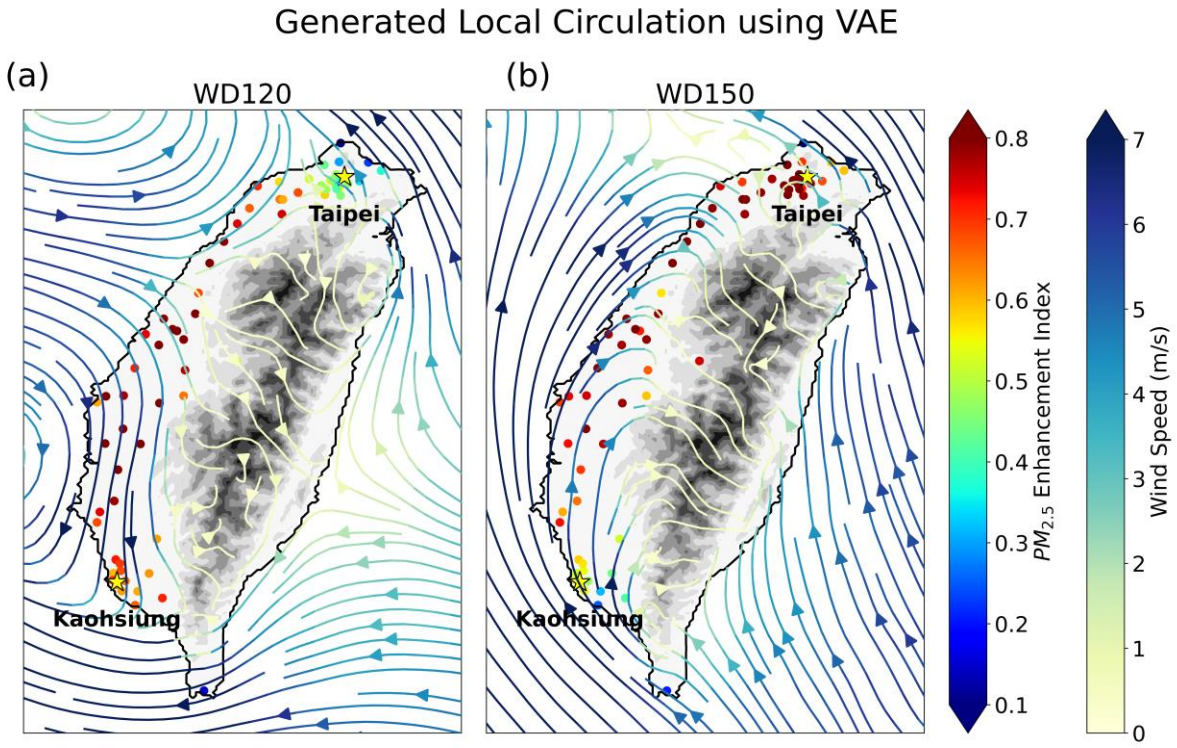

Fig. 7 (a) The generated local circulation (streamlines) and the observed local pollution enhancement index (colored dots) in Taiwan in the selected WD120 flow regime as depicted in Fig. 1a). (b) Same as (a) but in the selected WD150 flow regime. The $PM_{2.5}$ enhancement index and the definition of the WD120/WD150 are the same as depicted in Fig. 1b and 1c. The local circulations are generated from the reduced-order model derived from the VAE with the average synoptic wind speeds and directions of the selected days within WD120/WD150 are projected into the latent space.

As depicted in the introduction section, the bifurcation of the local $PM_{2.5}$ pollution enhancement scenarios implies a distinct change in local circulations between WD120 and WD150 synoptic flow regimes. By projecting the selected cases' mean wind direction and speed into the latent space of the VAE, the local circulations corresponding to WD120 and WD150 flow regimes can be generated using this reduced-order model. Figure 7 displays the generated local circulations along with the $PM_{2.5}$ enhancement indices under WD120 and WD150 flow regimes, as revealed in Fig. 1. The high-fidelity local circulations provide insights into the underlying pollutants transport processes that are responsible for the distinct local pollution deterioration. As displayed in Fig. 7a, a dipole of the lee vortices is identified in the local circulation under the WD120 flow regime. The local circulation over northern Taiwan is dominated by the cyclonic flow of the lee vortex located on the northern Taiwan Strait. On the other hand, the northerly on the central and south areas of the west plain of Taiwan can be attributed to the anti-cyclonic circulation of the other vortex located on the southern Taiwan Strait. As the major local emission sites are located on the west coastline of central and southern Taiwan, the local circulation on the west plain of Taiwan in Fig. 7a promotes the transport of the local pollutants both northward and southward, resulting in an overall deteriorated pollution scenario except for the north corner near Taipei. Notably, the sharp difference in $PM_{2.5}$

enhancement indices between the areas surrounding Taipei and the adjacent western regions aligns with the configuration of local circulations, where the lee vortex circulation causes southwesterly winds in this area to shift to southeasterly winds. Consequently, pollutants from central and southern Taiwan cannot reach Taipei owing to the prevailing southeasterly local flow in the areas around Taipei originating in eastern Taiwan, where pollutant emission sites are scarce.

As the synoptic flow regime shifts from WD120 to WD150, the local flow pattern turns into an elongated anti-cyclonic circulation on the west plain of Taiwan (Fig. 7b). The curved southerly flow, which later shifts to westerly over northern Taiwan, provides an efficient pathway for transporting pollutants from central and southern Taiwan to the Taipei metropolitan area. Compared with the scenarios of WD120 shown in Fig. 7a, the weaker southeasterly in Taipei areas also promotes a favorable environment for the accumulation of pollutants. Meanwhile, the strong southerly in Kaohsiung can alleviate the locally emitted pollution, resulting in a distinct scenario of the pollution distribution under the WD150 flow regime.

In this study, we demonstrate that this reduced order model is an effective tool for evaluating local circulations that provides a reliable physical examination of the local pollution scenarios. The bifurcation of the pollution scenarios can be physically interpreted through the sharp transition of the local circulations caused by the synoptic flow regime shifting from WD120 to WD150.

The AI downscaling approach proposed in this study can be further applied to the climate projection scenarios to shed light on the prediction of the local response to changes in the large-scale circulation in the warming climate. While the CMIP6 models' output represents the most up-to-date climate modeling data for a better understanding of the future of the climate system given internal climate variability uncertainties, the horizontal resolution of the CMIP6 GCMs, which is usually over 100 km, is still too coarse to be used in adaptation management at local scale such as Taiwan. Leveraging the reduced-order model, we can obtain high-fidelity representations of local circulation patterns given the projected synoptic flow regime scenarios in the coarser CMIP6 simulations, while achieving significant computational savings compared to traditional dynamical downscaling approaches. To demonstrate the capability of this framework, an example is provided using the large-scale flow regime change in TaiESM1 model output as the synoptic controlling physical parameters to apply the reduced-order model. By projecting the occurrence difference on the latent space, we can clearly identify the synoptic flow regimes change and the corresponding local circulation responses, as shown in Fig. 8. The heatmap in the latent space displayed in Fig. 8a indicates that the weak(about 4 m s^{-1}) easterly and the strong (about 10 m s^{-1}) southerly flow regimes are more profoundly increased under the SSP585 warming climate. By applying the reduced-order model to generate the local circulation based on these projected locations in the latent space, the local flow pattern can be evaluated as displayed in Fig 8b and 8c. The local circulation response of the strong southerly scenario (Fig 8b) displayed a flow pattern akin to the scenario of the WD150 scenario (Fig. 7b) with an elongated anticyclonic circulation along the west coast of Taiwan that promotes the local pollutants transport from central and southern Taiwan to the Taipei metropolitan area. On the other hand, the weak easterly scenarios induces a dipole of the lee vortices on the west of Taiwan. The cyclonic flow of the northern vortex promotes strong southeasterly winds over the areas around Taipei, while the center of the southern vortex locates at Kaohsiung indicates that the weak wind situation in Kaohsiung city might favors the pollutants accumulation.

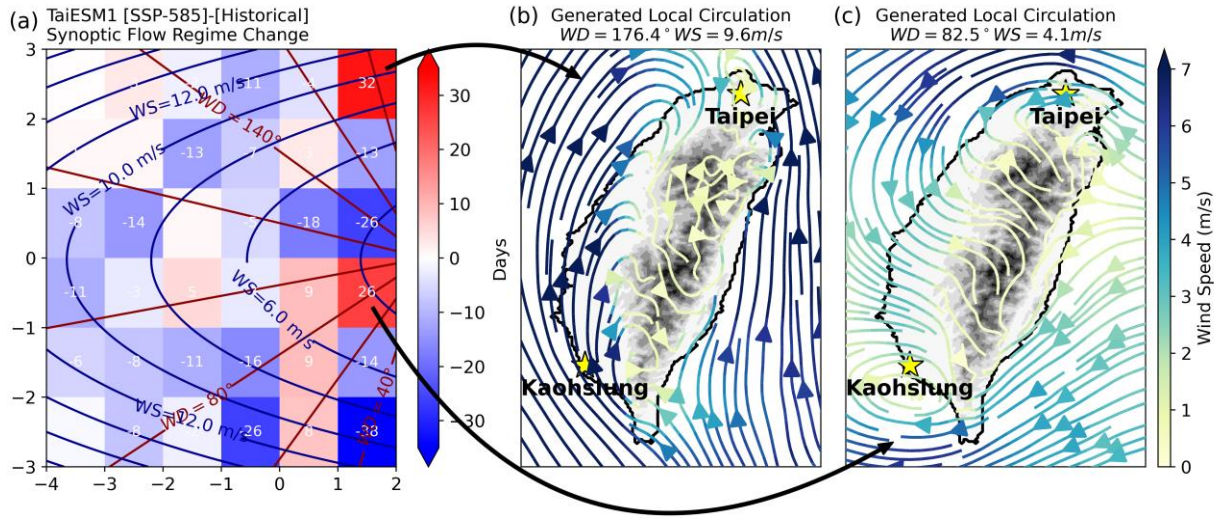

Fig. 8 (a) The projected synoptic flow regimes change from current climate to SSP585 warming scenario in TaiESM1 in the latent space. Two most increased flow regimes are selected to generate the corresponding local circulations indicating by the curved arrows as (b) the local circulation under the strong southerly and (c) the local circulation under the weak easterly. The correspondent synoptic wind speeds and directions are indicated in the titles of subfigures (b) and (c). The synoptic flow regime change is defined as below: we take the near-surface wind (at 1000 hPa) at the geographic location of Ishigaki island, Japan, as the synoptic flow regime upstream to Taiwan in the cold season (Oct. to Apr.) for a 20-year period in both of the historical (1990-2010) and SSP585 climate scenario(2079-2099) experiment data. After confining the wind direction between 30° and 180°, and excluding the sharp wind direction change around the nearby area of Taiwan as criteria for filtering out the strong synoptic weather system such as the front system, the flow regime change is calculated as the occurrence change of different flow regimes in these filtered days between the current climate and SSP858 warming scenario.

Examining the local circulation responses to the most possible increasing flow regimes above indicates that the two major cities of Taiwan, namely Taipei and Kaohsiung, could experience pollution deterioration from the local pollutant transport. The reduced-order model as an AI downscaling tool provides an instantaneous evaluation of the high-resolution local circulation given a specific synoptic flow regime. As a 48-hour semi-realistic simulation conducted in this study takes 9 hours on a 64-core computer to create 132 snapshots of the local circulations, it only takes 1.17 seconds for VAE to create the same local circulation ensembles. While the physical model simulation can provide a comprehensive evolution of Taiwan's 3-dimensional local circulation structure, we demonstrate that the reduced-order model can accelerate the evaluation of the surface local circulation by more than 27,000 times. It shows this framework's potential in assessing Taiwan's local circulation under multiple warming scenarios or in the diverse CMIP GCM simulation results. Our ongoing work is to characterize the local circulation response to East Asia's synoptic flow regime shift in CMIP6 multiple GCM members. The diversity of the local response in the spread of the CMIP6 climate projection can be examined through the reduced-order model. It is worth noting that this framework empowers the efficiency of the VAE model prediction to the storyline approach of representing the uncertainty in climate change proposed by Shephard et al. (2018). As the reduced-order model can

efficiently evaluate the local circulation, the uncertainty of the future local pollution events owing to the variability in the GCM projections can be isolated and evaluated. This advancement in modeling capabilities enables us to explore and understand the uncertainty of local weather phenomena in response to changing climate conditions with efficiency and accuracy. By utilizing this innovative approach, researchers can make more informed decisions regarding pollution control strategies and policy interventions to mitigate the environmental impacts of local pollution.

Furthermore, we emphasize that the explainable VAE framework introduced in this study has the potential to assess various weather regimes under climate change. With a clear physical connection established between synoptic controlling factors and specific local weather patterns, a series of ensemble LES experiments can be carried out focusing on the specific local weather regime that captures the various local responses to large-scale variability. By learning from this dataset, the reduced-order model of this specific weather regime can be constructed.

Acknowledgments

This study is supported jointly by Taiwan's NSTC through Grant 112-2111-M-002-015- and Grant NTU112L7832 to National Taiwan University.

Data Availability Statement

All code used to produce figures, along with the VAE model, training and validation scripts, and reconstruction results are available for download here: https://10.5281/zenodo.10086813. However, please note that due to file size limitations, we are unable to provide online access to the semi-realistic large ensemble simulations, the training dataset, and the TaiESM1 climate data. If you require access to the training dataset, please contact the authors directly. The figures in this study were generated using Matplotlib version 3.5.1 (Hunter, 2007), which is available under the Matplotlib license at https://doi.org/10.5281/zenodo.5773480.

References

Behrens, G., Beucler, T., Gentine, P., Iglesias-Suarez, F., Pritchard, M., & Eyring, V. (2022). Non-Linear Dimensionality Reduction With a Variational Encoder Decoder to Understand

Convective Processes in Climate Models. Journal of Advances in Modeling Earth Systems, 14(8), e2022MS003130. https://doi.org/10.1029/2022MS003130

Beucler, T., Gentine, P., Yuval, J., Gupta, A., Peng, L., Lin, J., et al. (2021, December 14). Climate-Invariant Machine Learning. arXiv. https://doi.org/10.48550/arXiv.2112.08440

Bhatia, S., Jain, A., & Hooi, B. (2021, March 15). ExGAN: Adversarial Generation of Extreme Samples. arXiv. https://doi.org/10.48550/arXiv.2009.08454

Bi, K., Xie, L., Zhang, H., Chen, X., Gu, X., & Tian, Q. (2023). Accurate medium-range global weather forecasting with 3D neural networks. Nature, 619(7970), 533–538. https://doi.org/10.1038/s41586-023-06185-3

Chang, Y.-H., Chen, W.-T., Wu, C.-M., Moseley, C., & Wu, C.-C. (2021). Tracking the influence of cloud condensation nuclei on summer diurnal precipitating systems over complex topography in Taiwan. Atmospheric Chemistry and Physics, 21(22), 16709–16725. https://doi.org/10.5194/acp-21-16709-2021

Chien, M.-H., & Wu, C.-M. (2016). Representation of topography by partial steps using the immersed boundary method in a vector vorticity equation model (VVM): VVM PARTIAL STEP. Journal of Advances in Modeling Earth Systems, 8(1), 212–223. https://doi.org/10.1002/2015MS000514

Daw, A., Karpatne, A., Watkins, W., Read, J., & Kumar, V. (2017, October 31). Physics-guided Neural Networks (PGNN): An Application in Lake Temperature Modeling. arXiv. https://doi.org/10.48550/arXiv.1710.11431

Eyring, V., Bony, S., Meehl, G. A., Senior, C. A., Stevens, B., Stouffer, R. J., & Taylor, K. E. (2016). Overview of the Coupled Model Intercomparison Project Phase 6 (CMIP6) experimental design and organization. Geoscientific Model Development, 9(5), 1937 - 1958. https://doi.org/10.5194/gmd-9-1937-2016

Goodfellow, I. J., Pouget-Abadie, J., Mirza, M., Xu, B., Warde-Farley, D., Ozair, S., et al. (2014). Generative Adversarial Networks. arXiv. https://doi.org/10.48550/arXiv.1406.2661

Hsieh, M.-K., Chen, Y.-W., Chen, Y.-C., & Wu, C.-M. (2022). The Roles of Local Circulation and Boundary Layer Development in Tracer Transport over Complex Topography in Central Taiwan. Journal of the Meteorological Society of Japan. Ser. II, 100(3), 555–573. https://doi.org/10.2151/jmsj.2022-028

737 Hsu, T.-H., Chen, W.-T., Wu, C.-M., & Hsieh, M.-K. (2023). The Observation-Based Index to
738 Investigate the Role of the Lee Vortex in Enhancing Air Pollution over Northwestern Taiwan.
739 Journal of Applied Meteorology and Climatology, 62(3), 427–439.
740 https://doi.org/10.1175/JAMC-D-22-0102.1
741 Hunter, J. D. (2007). Matplotlib: A 2D Graphics Environment. Computing in Science &
742 Engineering, 9(3), 90–95. https://doi.org/10.1109/MCSE.2007.55
743 Jung, J.-H., & Arakawa, A. (2008). A Three-Dimensional Anelastic Model Based on the
744 Vorticity Equation. Monthly Weather Review, 136(1), 276–294.
745 https://doi.org/10.1175/2007MWR2095.1
746 Karpatne, A., Atluri, G., Faghmous, J. H., Steinbach, M., Banerjee, A., Ganguly, A., et al.
747 (2017). Theory-Guided Data Science: A New Paradigm for Scientific Discovery from Data.
748 IEEE Transactions on Knowledge and Data Engineering, 29(10), 2318–2331.
749 https://doi.org/10.1109/TKDE.2017.2720168
750 Kingma, D. P., & Welling, M. (2019). An Introduction to Variational Autoencoders. Foundations
751 and Trends® in Machine Learning, 12(4), 307–392. https://doi.org/10.1561/2200000056
752 Kingma, D. P., & Welling, M. (2022, December 10). Auto-Encoding Variational Bayes. arXiv.
753 Retrieved from http://arxiv.org/abs/1312.6114
754 Klemmer, K., Saha, S., Kahl, M., Xu, T., & Zhu, X. X. (2021, April 26). Generative modeling of
755 spatio-temporal weather patterns with extreme event conditioning. arXiv.
756 https://doi.org/10.48550/arXiv.2104.12469
757 Kuo, K.-T., & Wu, C.-M. (2019). The Precipitation Hotspots of Afternoon Thunderstorms over
758 the Taipei Basin: Idealized Numerical Simulations. Journal of the Meteorological Society of
759 Japan. Ser. II, 97(2), 501–517. https://doi.org/10.2151/jmsj.2019-031
760 Lai, H.-C., & Lin, M.-C. (2020). Characteristics of the upstream flow patterns during PM2.5
761 pollution events over a complex island topography. Atmospheric Environment, 227, 117418.
762 https://doi.org/10.1016/j.atmosenv.2020.117418
763 Lam, R., Sanchez-Gonzalez, A., Willson, M., Wirnsberger, P., Fortunato, M., Pritzel, A., et al.
764 (2022, December 24). GraphCast: Learning skillful medium-range global weather forecasting.
765 arXiv. https://doi.org/10.48550/arXiv.2212.12794

Lee, W.-L., Wang, Y.-C., Shiu, C.-J., Tsai, I. -chun, Tu, C.-Y., Lan, Y.-Y., et al. (2020). Taiwan Earth System Model Version 1: description and evaluation of mean state. Geoscientific Model Development, 13(9), 3887–3904. https://doi.org/10.5194/gmd-13-3887-2020

Lin, C.-Y., Sheng, Y.-F., Chen, W.-C., Chou, C. C. K., Chien, Y.-Y., & Chen, W.-M. (2021). Air quality deterioration episode associated with a typhoon over the complex topographic environment in central Taiwan. Atmospheric Chemistry and Physics, 21(22), 16893–16910. https://doi.org/10.5194/acp-21-16893-2021

Oliveira, D. A. B., Diaz, J. G., Zadrozny, B., & Watson, C. (2021, July 30). Controlling Weather Field Synthesis Using Variational Autoencoders. arXiv. https://doi.org/10.48550/arXiv.2108.00048

Pathak, J., Subramanian, S., Harrington, P., Raja, S., Chattopadhyay, A., Mardani, M., et al. (2022, February 22). FourCastNet: A Global Data-driven High-resolution Weather Model using Adaptive Fourier Neural Operators. arXiv. https://doi.org/10.48550/arXiv.2202.11214

Shamekh, S., Lamb, K. D., Huang, Y., & Gentine, P. (2022). Implicit learning of convective organization explains precipitation stochasticity (preprint). Atmospheric Sciences. https://doi.org/10.1002/essoar.10512517.1

Shen, Z., Sridhar, A., Tan, Z., Jaruga, A., & Schneider, T. (2022). A Library of Large-Eddy Simulations Forced by Global Climate Models. Journal of Advances in Modeling Earth Systems, 14(3), e2021MS002631. https://doi.org/10.1029/2021MS002631

Shepherd, T. G., Boyd, E., Calel, R. A., Chapman, S. C., Dessai, S., Dima-West, I. M., et al. (2018). Storylines: an alternative approach to representing uncertainty in physical aspects of climate change. Climatic Change, 151(3), 555–571. https://doi.org/10.1007/s10584-018-2317-9

Wang, C., Tang, G., & Gentine, P. (2021). PrecipGAN: Merging Microwave and Infrared Data for Satellite Precipitation Estimation Using Generative Adversarial Network. Geophysical Research Letters, 48(5), e2020GL092032. https://doi.org/10.1029/2020GL092032

Wilby, R. L., & Dessai, S. (2010). Robust adaptation to climate change. Weather, 65(7), 180–185. https://doi.org/10.1002/wea.543

Wu, C.-M., & Arakawa, A. (2011). Inclusion of Surface Topography into the Vector Vorticity Equation Model (VVM): INCLUSION OF SURFACE TOPOGRAPHY INTO THE VVM. Journal of Advances in Modeling Earth Systems, 3(2), n/a-n/a. https://doi.org/10.1029/2011MS000061

Wu, C.-M., Lin, H.-C., Cheng, F.-Y., & Chien, M.-H. (2019). Implementation of the Land Surface Processes into a Vector Vorticity Equation Model (VVM) to Study its Impact on Afternoon Thunderstorms over Complex Topography in Taiwan. Asia-Pacific Journal of Atmospheric Sciences, 55(4), 701–717. https://doi.org/10.1007/s13143-019-00116-x

Zadrozny, B., Watson, C. D., Szwarcman, D., Civitarese, D., Oliveira, D., Rodrigues, E., & Guevara, J. (2021, February 5). A modular framework for extreme weather generation. arXiv. https://doi.org/10.48550/arXiv.2102.04534